Adaptive anisotropic integration scheme for high-order fictitious domain methods: Application to thin structures

Grégory Legrain, Nicolas Moes

Adaptive anisotropic integration scheme for high-order fictitious domain methods: Application to thin structures

G.Legrain and N. Moës

GeM Institute
GeM Institute UMR CNRS 6183
École Centrale de Nantes / Université de Nantes / CNRS,
1 Rue de la Noë, BP92101, 44321 Nantes, France.

Preprint submitted to: International Journal for Numerical Methods in Engineering

Adaptive anisotropic integration scheme for high-order fictitious domain methods: Application to thin structures

G. Legrain[1⋆], N. Moës[1]

[1] *GeM Institute, UMR CNRS 6183, École Centrale de Nantes, Université de Nantes, France*

SUMMARY

A novel integration scheme is proposed for fictitious domain finite element methods. It relies on the use of a surface tracking strategy based on anisotropic mesh adaptation. Thanks to an error estimator, the method builds iteratively an adapted anisotropic mesh which is refined near the geometrical interface, and elongated in the direction of small curvature. This strategy allows to decrease the integration cost which can be problematic for high order fictitious domain methods. In addition, it opens the possibility for the creation of unfitted solid shell strategies that can be used for the treatment of thin structures. Numerical studies show that the method leads to promising results for both integration cost and behaviour with respect to locking.

Preprint submitted to: International Journal for Numerical Methods in Engineering

KEY WORDS: X-FEM; high-order; fictitious domain; anisotropic meshing, solid-shell, shell, plates, beams

1 Introduction

Fictitious domain methods have recently gained more attention because of their favourable properties to conduct design-through analysis [1]. Indeed, this concept aims at creating more efficient part designs thanks to the tight relationship between CAD and analysis. It allows designers to draw parts with mechanical efficiency in mind. Such strategies require a seamless transition between geometrical representation (CAD surfaces for instance) and analysis. Isogeometric analysis [2] was proposed with this objective in mind, and has proved to be a very efficient method. However, meshing is still necessary: it requires clean CAD surfaces, a volumetric parametrization of the solid [2] (whereas the CAD only deals with surface representation), and also trimming-free surfaces [3, 4] , although this last topic is the subject of numerous recent works [5, 3, 6, 7, 8]. Thanks to their ability to use unfitted meshes, fictitious domain methods are also an answer to

⋆Correspondence to: G. Legrain. E-Mail: gregory.legrain@ec-nantes.fr

this objective. Albeit known for decades [9], fictitious domain methods have been recently revisited in the context of the X-FEM [10, 11, 12, 13, 14, 15], Cartesian grids [16] for low-order approximations, and also in the context of higher order approximations with the introduction of the Finite Cell method [17, 18, 19, 20, 21, 22]. This method can be seen as a hybrid between p-fem and fictitious domains, retaining advantages of both (i.e. exponential convergence for smooth solutions without meshing burden). The difficulty shared by these methods lies in the cost and accuracy of the integration of the weak form, as meshing difficulties are transferred into the proper integration of this quantity. For low order approximations, the geometrical error is usually of higher order than the approximation error: "coarse" polygonal discretizations are sufficient if their size is similar to the size of the approximation elements. Unfortunately, it is not the case for higher-order approximations where the geometrical error has to be kept smaller than the approximation error (which decreases exponentially). Sub-grid integration strategies have been proposed in the context of both Finite Cell [19] and higher-order X-FEM [23, 14]. In the first case, integration points in the sub-grid are filtered based on their location whereas a fine triangulation of the surface is built for the latter. These two approaches are satisfactory, but can require quite large computational resources for the integration due to the large number of integration points, unless pre-computed strategies like in [24] are considered. Recent contributions [25, 26, 27, 28] propose to use moment fitting techniques [29, 30, 31] to construct integration rules on the fly. Blended integration cell methods have also been proposed in order to decrease the integration cost thanks to large mapped integration cells [32, 33, 34, 35, 36, 37]. All these methods can improve the efficiency of the integration although the most robust method remains the sub-grid based integration. In this paper, we propose an efficient variant of sub-grid integration rules that improves its numerical efficiency in low-curvature areas, and also evaluate new possibilities opened by this method. In particular, we will focus on the treatment of slender structures that are typically challenging for this family of methods, as the size of the integration cells must be smaller than the thickness of the structure. The method is based on an anisotropic mesh adaptation strategy [38] which consists in optimizing not only mesh density, but also elements shape. A large literature is devoted to this topic, interested reader is referred to [39, 40, 41, 42, 43, 44, 45, 46, 47] to name a few. The adaptation strategy that is considered here is relying on the metric tensor proposed by Coupez [48, 49]. This approach is based on the level-set representation of the interface and ensures a proper representation of this surface with a minimum number of elements. The resulting mesh is naturally refined near large curvature regions and elongated along low curvature zones. The proposed method enables to decrease the number of integration points, but can also effectively capture the very thin areas of the domain.

We thus propose to study the performances of fictitious domain methods for this family of problems, which are generally approximated by means of shell and plate elements. These models are computationally efficient as they require very few dofs through the discretization of the mid-surfaces. However this meshing step can be tedious and these elements are unable to represent complex through the thickness behaviours, and lead to modelization issues for contact and in plate to solid transition zones. Thereby leading

researchers to develop so-called solid-shell elements that are based on displacement-only kinematic, with one layer of element across the thickness in order to improve their computational efficiency. Such methods can effectively model thick and thin areas, large strain problems, and capture through the thickness phenomena (especially for nonlinear problems). The meshing step is also alleviated (although not removed). Naive solid-shell elements are unfortunately subjected to membrane and shear locking so that adapted formulations relying generally on assumed strain formulations with reduced integration and hourglass control are usually used [50, 51, 52, 53]. This family of methods have been recently extended in the context of isogeometric analysis by Bouclier et al. [54, 55, 56]. In addition, note also the contribution of Düster et al. [57] who proposed effective p-fem formulations for plates en shells. All these methods rely on the meshing of the structure which can be tedious for complex industrial parts. We therefore propose to evaluate the performances of high-order fictitious domain methods in this context in order to combine both the performances of fictitious domains (meshing ease) and high-order methods (exponential convergence). The proposed method can be seen as an extension of the method proposed in [15].

The remainder of the paper is organized as follows: first, the anisotropic mesh adaptation method used in this contribution is introduced and illustrated. Then, its coupling with fictitious domain methods is presented. In a second part, the strategy is assessed both with respect to the integration cost and with respect to solid-shell applications. The method is finally verified against common shell benchmarks in both 2D and 3D.

2 Fictitious domain strategies based on anisotropic mesh adaptation

2.1 Motivation

The use of fictitious domain methods for thin structures can be traced back to only two contributions [18, 15]. The Shell Finite Cell [18] consists in mapping a 2D parametric space onto a thin 3D space. The Finite-Cell method is used in the parametric space to streamline the representation of complex geometrical features. In [15], a moderate order (quadratic) X-FEM approximation in the physical space was used. This approach requires a large number of approximation elements in order to be able to resolve the thickness of the structures and represent geometrical edges with a good accuracy (see Figure 1 (a)). Increasing the order of the approximation and using sub-grid level-sets [23, 14] was also advocated, but led to a large amount of integration points (see Figure 1 (b)). Indeed, the size of the geometrical cells must be smaller than the thickness of the structure so that it can be represented. In the case of mixed slender and massive zones, it either leads to massive integration costs or the disappearance of the slender zones, depending on the user-defined size of these cells. In addition, the edges of the geometry are lost as their scale is below the geometrical resolution of the geometrical mesh. The objective here is to propose an alternative geometrical representation strategy for

such applications. This approach, which is based on anisotropic mesh adaptation, is top to bottom and allows to capture both small and large geometrical features. It should also be very efficient for representing low-curvature areas that are common for industrial designs.

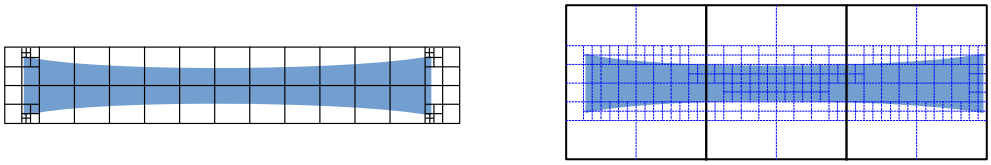

(a) (b)

Figure 1: Strategies for thin structures (thick lines: approximation elements, dashed lines: geometrical elements): (a) moderate order X-FEM [15]; (b) sub-grid level-set [23, 14].

2.2 Anisotropic mesh adaptation for level-sets

The objective of anisotropic mesh adaptation is to construct a mesh for which the approximation error is uniform and below a given threshold. The main difference with classical (isotropic) mesh adaptation lies in the shape of the elements. The only parameter for isotropic mesh refinement is the element size field across the structure of interest, whereas anisotropic mesh refinement allows to specify the size of the elements in all the directions to achieve error uniformity. If the solution has a slow evolution in one direction, then elements size can be increased along this direction without any particular influence on the error level. In the example presented in Figure 2, the error is obviously lower for the anisotropic mesh for a given number of vertices.

The method relies on the construction of a metric tensor, $\boldsymbol{\mathcal{M}}(\mathbf{x})$ which is used by the mesher to redefine the way lengths are computed depending on the direction. This metric tensor is usually obtained on an element-basis [58], but in practice it is more convenient to work with nodal metrics as it leads to continuous metric fields in space. These continuous fields greatly simplify metric interpolation and extrapolation operations. The approach considered in this contribution follows this alternative path, and relies directly on a nodal metric (without any post-processing of elementary quantities). This approach was proposed in [48], and depends on a so called length-distribution tensor which is derived from a statistical concept introduced in polymer science [59]. The originality lies in the construction of the metric, and the associated *edge-based* error estimator which avoids complex Hessian reconstructions like those proposed in [46, 60]. In the case of level-sets, the target region for the adaptation process is not the whole domain, but the zone near the iso-zero. This is achieved here by working with the regularized Heaviside function of the level-set:

$$u_\varepsilon(\mathbf{x}) = \varepsilon \tanh\left(\frac{\phi(\mathbf{x})}{\varepsilon}\right). \tag{1}$$

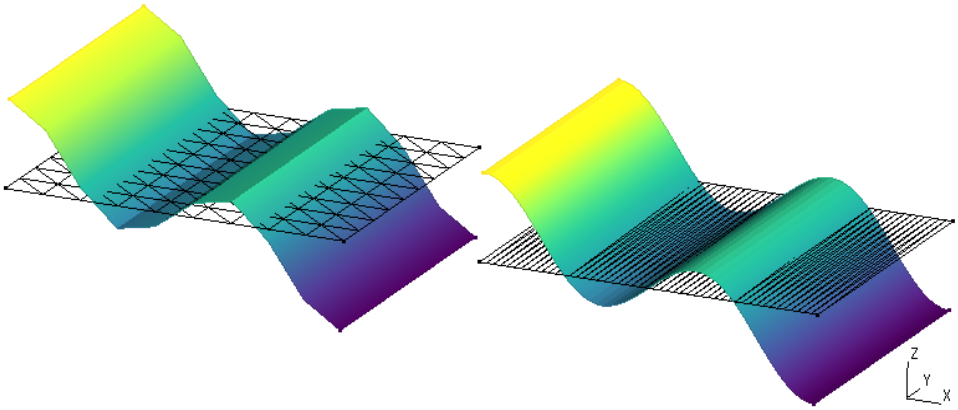

Figure 2: Interpolation of the function $\sin(x\pi/2)\cos(x\pi)$ on two meshes composed of 100 nodes. Left: isotropic mesh, right: anisotropic mesh.

This function is a proper choice as it is C^∞ and concentrates the interpolation error solely in the vicinity of the iso-zero.

The features of the metric are now illustrated for some 2D examples. We only focus on some qualitative illustrations, in order to highlight the main features of the adaptation procedure, as it has already been deeply studied in [48, 61, 49]. To this end, different geometries are considered: (i) a plane interface, (ii) a circular interface and (iii) a corner interface. The first geometry involves no curvature, the second has a constant one, and the third one a varying curvature. Adapted meshes for different values of regularization parameter ε are presented in Figure 3.

As expected, the elements are aggregated in a band of length $\simeq 2\sqrt{2}\varepsilon$ and elongated along the directions with small curvature. In regions of large curvature (near the apex of the corner), then the elements are isotropic. In addition, it should be noted that decreasing ε allows to master the geometrical accuracy of the discrete geometry, as the approximated iso-zero lies in the $2\sqrt{2}\varepsilon$ band around the real iso-zero.

2.3 Anisotropic mesh adaptation for fictitious domains

The anisotropic integration mesh which is generated by the anisotropic mesh adaptation procedure has to be linked to the approximation mesh, so that the weak formulation can be integrated properly. In the case of sub-grid level-sets or with the Finite-Cell, this connection step is trivial as the integration cells are embedded within the approximation mesh (see Figure 1 (b)). In the present case, an ad-hoc strategy has to be proposed as the anisotropic integration mesh is completely unrelated to the approximation mesh (see Figure 4(a)).

In order to build a set of embedded integration cells from the anisotropic mesh, we choose to focus on regular quadrangular or hexahedral approximation meshes. Then, the regular pattern of this approximation mesh is used to slice the integration mesh along

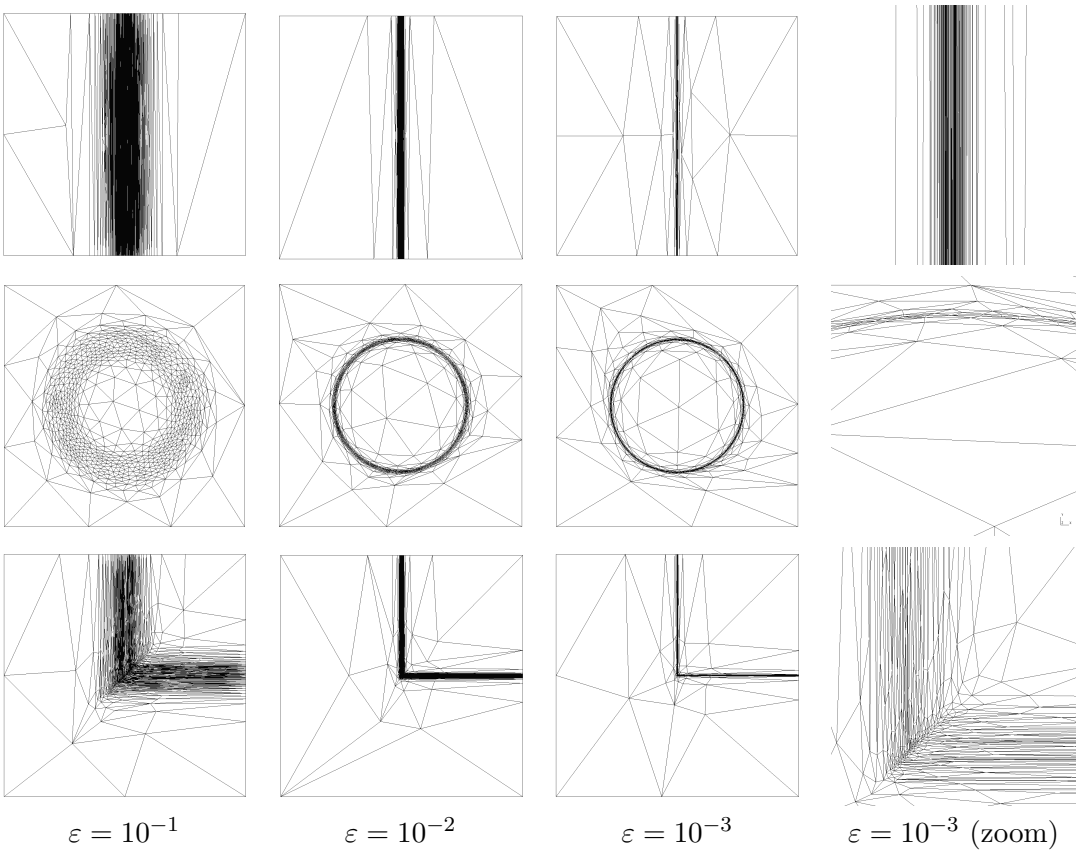

Figure 3: Illustration of the anisotropic procedure for various interfaces: straight (509, 513, 517 nodes), circular (765, 787, 792 nodes) and corner (751, 759, 763 nodes)

the boundaries of the approximation elements, thereby leading to a set of embedded anisotropic integration cells ((see Figure 4(b)). This operation can be done robustly and efficiently by re-using level-set slicing routines. Note however that this strategy is not restricted to regular grids and could be easily extended to octree-based approximation meshes, applying it recursively in the leaves of the octree.

In a last step (Figure 4(c)), integration cells are only kept for the approximation elements containing the interface to be captured. This allows to restrict integration effort only where it is needed. After this procedure, one obtains a suitable integration mesh for the fictitious domain procedure.

Note that this slicing procedure leads to an increase in the number of integration cells, which could be balanced by only retaining the narrow-band of the anisotropic integration mesh. The development of such a strategy is currently in progress. Throughout this contribution, all the integration cells are equipped with full Gauss quadrature rules, designed so that the polynomial quantities involved in the formulation can be evaluated exactly. This leads to a large number of integration points, but one could also use a non-uniform quadrature rule, such as the one proposed in [62]. It consists in lowering the number of integration points for the very small cells that are created near the interfaces in order to further improve the numerical efficiency of the integration.

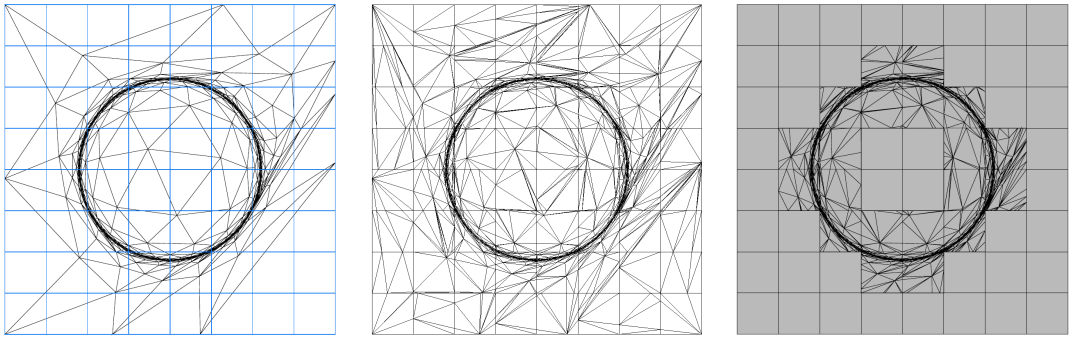

(a) (b) (c)

Figure 4: (a) Approximation mesh (thick lines) and integration mesh (thin lines); (b) Sliced integration mesh; (c) Resulting integration cells.

2.4 Comparison with octree adaptation

This section is devoted to the characterization of the strengths and weaknesses of the anisotropic procedure compared to the classical octree-based strategy, in terms of geometrical accuracy only. The influence of this geometrical accuracy on the solution of the physical problem is studied in Section 3.1. The two methods are compared for fixed level-sets, by measuring their geometrical accuracy with respect to the number of nodes

in the meshes they produce. Given a level-set $\phi(\mathbf{x})$ and a mesh, the (absolute) geometrical error $\mathcal{E}^g$ associated to the mesh is defined as the integral of the distance between the discrete iso-zero of the level-set Γ^h and the exact iso-zero. This quantity can be evaluated easily when the exact level-set of the problem is known:

$$\mathcal{E}^g = \int_{\Gamma^h} |\phi(\mathbf{x})| d\Gamma. \tag{2}$$

We study the compared evolution of this error between octree and anisotropically adapted meshes. Throughout this section, octree and anisotropic results are depicted with solid and dashed lines respectively. Moreover, these curves share similar ticks for a given geometry. First, circular interfaces are considered with increasing radii, from 0.05 to 5 (see Figure 5 (a)). Octree meshes were generated by changing their depths from 5 to 10, and the anisotropic meshes were constructed with the same target number of nodes. Figure 5 (b) shows that the performance of these two methods are similar, and that

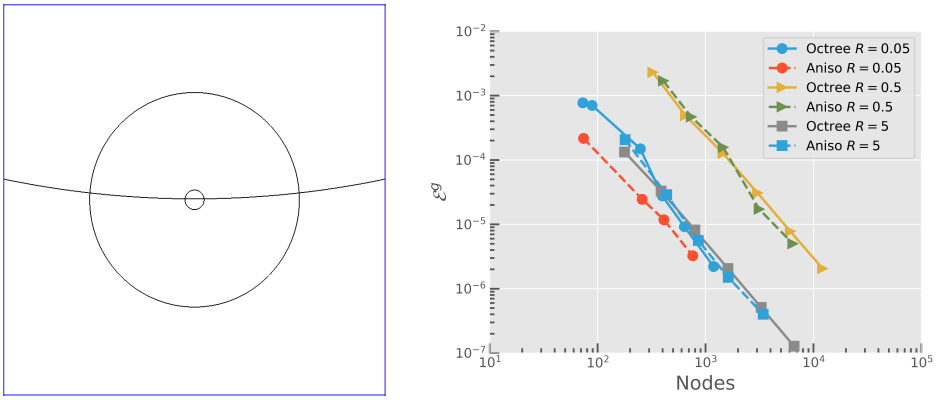

(a) (b)

Figure 5: Geometrical convergence. (a): Domain ($[-1, 1]^2$) and circular interfaces ($R = 0.05, 0.5, 5$); (b): Convergences: octree: thick lines, anisotropic: dashed lines.

it is not influenced by the curvature of the curve. This can be explained by the fact that in this case, the error is already homogeneous around the interface for isotropic meshes (the anisotropic strategy also tends to create isotropic element in this case, see Figure 3). Then, the case of a geometry mixing low and large curvature is considered in Figure 6 (a). The interface is obtained by the intersection of two off-centred circular level-sets of varying radii. The corresponding interface tends to a straight corner when the radius of the circles is increased. From the convergence study presented in Figure 6 (b), we can draw the following conclusions: (i) The presence of large and low curvature areas it better handled by the anisotropic approach. This stems from the fact that the anisotropic adaptation method is able to optimize the mesh when the geometrical error is non uniformly distributed in the domain, whereas the uniform size of the elements generated by the octree cannot. (ii) The larger the discrepancy between the

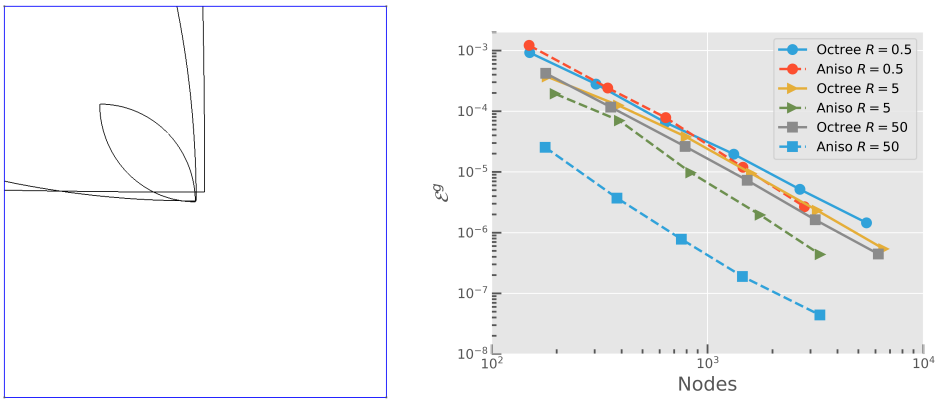

(a) (b)

Figure 6: Geometrical convergence. (a): Domain ($[-1, 1]^2$) and interfaces ($R = 0.5, 5, 50$); (b): Convergences: octree: thick lines, anisotropic: dashed lines.

low and large curvature areas, the better the performances of the anisotropic method. (iii) The efficiency of the anisotropic algorithm is at least on par with the octree scheme.

Finally, note that the performances of the anisotropic strategy are hindered by the layers of elements in the zones near the interface, as they do not contribute to the improvement of the geometrical accuracy. Methods making use of the narrow-band only may further improve its performances (more than for the octree).

3 Numerical examples

The numerical examples are divided in two parts: in the first one, the performance of the proposed approach is assessed with respect to the ratio between the cost of the numerical integration and the accuracy. In a second part, the potential of the use of such approach is highlighted in the case of the treatment of thin structures.

3.1 Integration cost

In the previous section, the parameters that influence the geometrical performances of the anisotropic adaptation scheme were studied. We focus now on the implications of these conclusions when dealing with physical problems. The objective of this section is to study to what extent do the geometrical conclusions extend to full calculations.

3.1.1 Circular Interface

Consider an infinite plate with a circular hole in its center which is loaded in uniaxial tension $\sigma_\infty = 1.0\,\text{MPa}$ along $\mathbf{x}$ axis (see Figure 7). The analytical solution of this prob-

lem is given in [63] and is used here as a reference solution for error monitoring. Only a square of length $L = 2.0\,\text{mm}$ with a circular hole of radius $a = 0.55\,\text{mm}$ at its center is considered here. Finally, tractions computed from the exact solution are applied on the boundary of the domain, and three dofs are prescribed to zero in order to avoid rigid body motion. The exact solution of this finite problem is therefore the same as the exact solution inside the boundary. Young's modulus is set to 1.0 MPa, and Poisson's ratio to 0.3. A p-convergence study is performed for $p = 1$ to 12, and the error in the energy norm is monitored with respect to the number of dofs and integration points. The approximation mesh is composed of 2×2 quadrangular elements with Legendre hierarchical shape functions. Typical integration meshes are depicted in Figure 8. In the octree case, the influence of the quality of the integration is presented in Figure 9 with $h_g = h/16$ and $h_g = h/64$ near the interface (where h_g stands for the size of the elements in the geometrical mesh crossed by the interface). This typical convergence curve highlights the interplay between geometrical and approximation errors. We now restrict ourselves to the coarsest mesh, and these results are compared with those obtained using anisotropic integration meshes. These meshes were designed so that the number of integration cells is similar between the two methods. With such coarse meshes (see Figure 10), the anisotropic regularization parameter is set to $3.\,10^{-2}$. The convergence curves corresponding to these three integration meshes are depicted in Figure 11. If one compares the convergence with respect to the number of dofs, then one can see that the behaviour of the anisotropic integration mesh is similar to the one of the octree, even if better error levels can be obtained. More interesting is the convergence with respect to the number of integration points, as these curves represent the integration effort which is required to attain a given error level. It is shown that for a similar number of integration points, the anisotropic integration performs better than the octree one (see the curve "Aniso 259"): for the same number of integration points, the asymptotic error is divided by 2. Before the point where the geometrical error exceeds the approximation error, the two schemes perform the same. More interestingly, the coarsest anisotropic mesh (curve "Aniso 212") constantly outperforms the octree one: it is more efficient and gives more accurate results than the octree. These results, however, do not show the full potential of the method: Indeed, it was shown in Section 2.4 that in the case of a constant curvature, the performances of the anisotropic strategy are similar to the performances of the octree. Hence, a case with non-uniform curvature is considered in the next section.

3.1.2 Varying curvature interface

Consider the example presented in Figure 12. It represents a square of length 2×2 with a square hole of length $a = 0.8$ at the center of the frame. A Laplace equation is solved on this domain: source and flux are prescribed respectively in the domain and on the boundary so that the solution is $u(x, y) = \cos(\pi x/a)\,\sin(\pi y/a)$ (see Figure 12 for a sketch). The problem is solved by means of a 4×4 mesh which is presented in Figure 12. The geometry is either represented using an octree mesh or using an anisotropic mesh.

A first solution is obtained by means of an octree mesh with $h_g = h/32$: in this case,

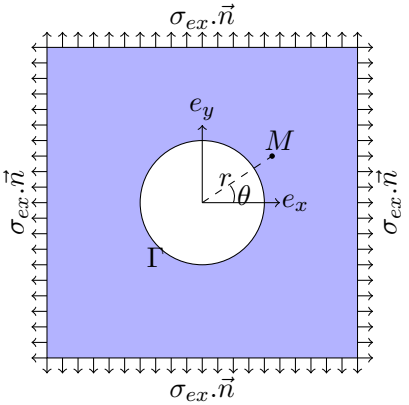

Figure 7: Infinite plate with a hole submitted to uniaxial tension: geometry and approximation mesh.

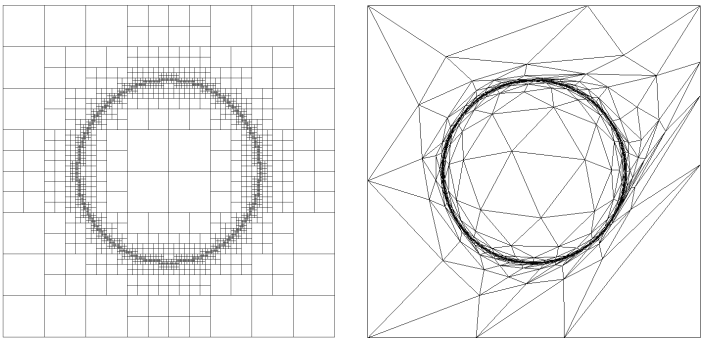

Figure 8: Typical integration meshes: octree (left) and anisotropic, $\varepsilon = 10^{-6}$ (right)

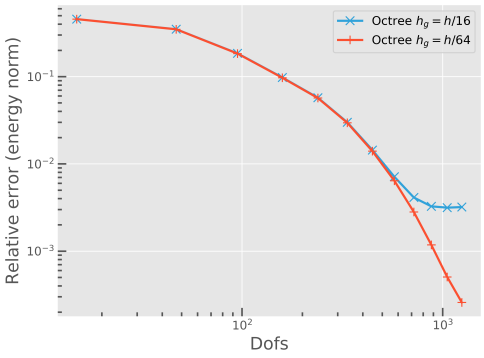

Figure 9: Typical convergence curve (octree integration)

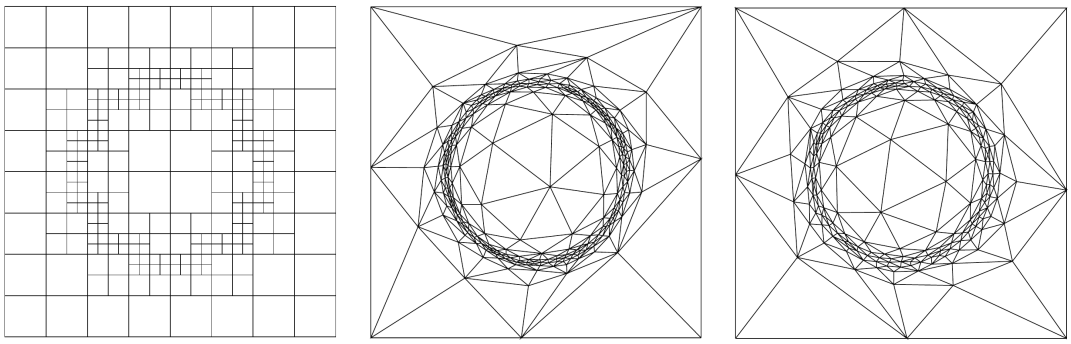

Figure 10: Similar integration meshes (left to right): octree with $h_g = h/16$, anisotropic with 259 elements, anisotropic with 212 elements.

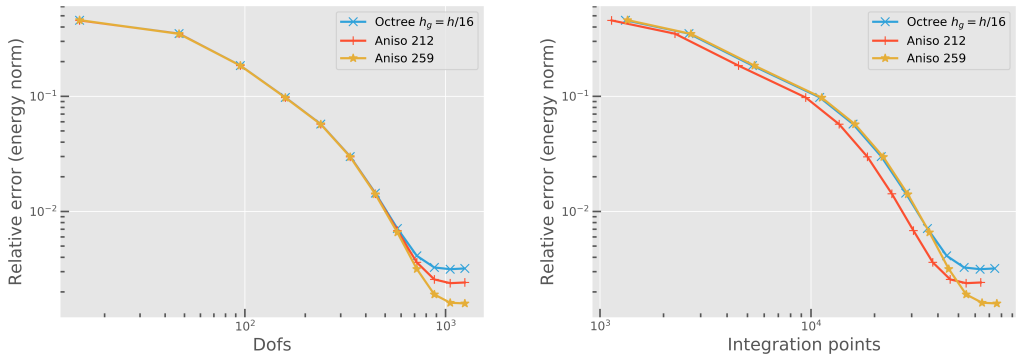

(a) (b)

Figure 11: Comparison of the performances of octree and anisotropic integration meshes. Left: with respect to the number of dofs, Right: with respect to the number of integration points.

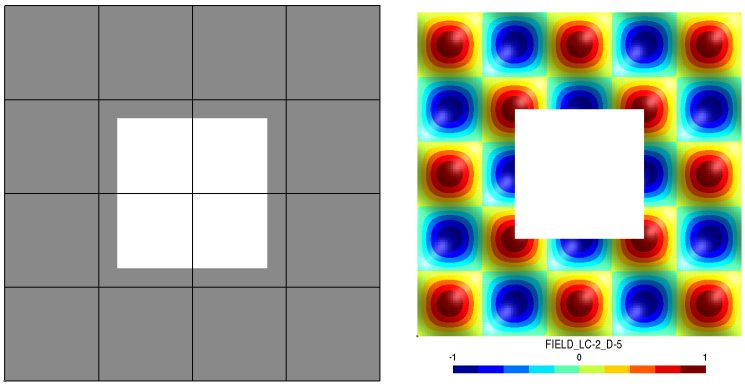

Figure 12: Kinked interface: left, Mesh and domain; right, exact solution.

the geometry is represented exactly, as the corners of the square are located on the edges of the elements. A p-convergence is conducted, from $p = 1$ to 8, and it can be seen in Figure 14(a) that an exponential convergence is obtained in the energy norm. This is consistent, since the geometry is captured exactly and the solution is regular. The center of the hole is now moved to $(-0.18, -0.09)$, so that it is not located on the edges of the elements.

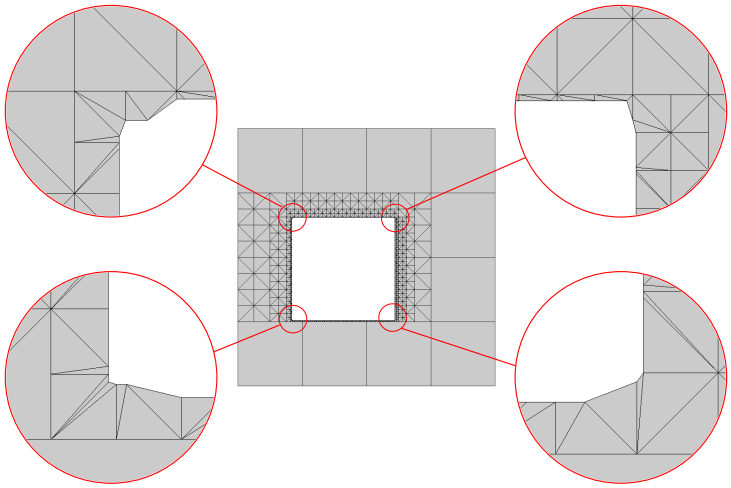

Figure 13: Integration cells for an octree integration scheme with $h_g = h/32$.

The corresponding integration mesh is shown in Figure 13 (1168 nodes): the error in the perimeter length of the square is 0.5% in this case. It can be seen in Figure 14(a) that this geometrical error causes a severe loss of accuracy as the convergence stagnates at a level of 0.4%.

Anisotropic integration is now considered (with a regularization parameter of 10^{-4})

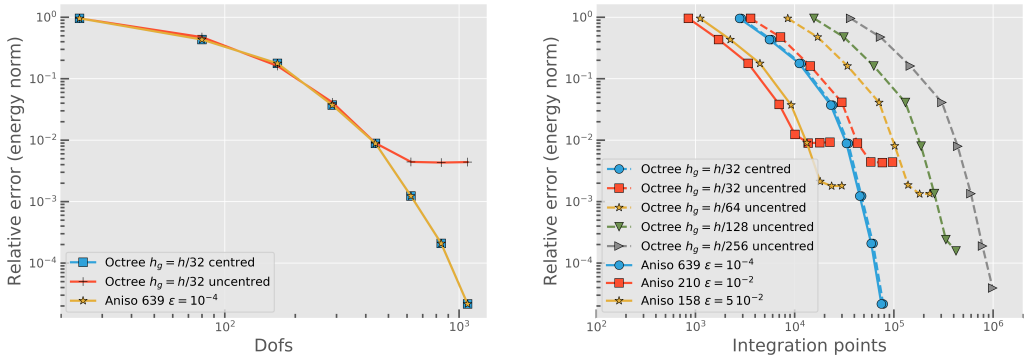

(a) (b)

Figure 14: Error in the energy norm. (a) with respect to dofs, (b) with respect to the number of integration points.

which leads to the 639 nodes mesh presented in Figure 15. Using this mesh for the geometry enables to recover the exponential convergence for all the polynomial range. However, we are also interested in the efficiency of the integration scheme. Various integration schemes are compared in Figure 14(b), where the error in the energy norm is plotted with respect to the number of integration points. One can see that if an octree mesh is used, then error levels similar to the anisotropic mesh can be obtained only by selecting very fine elements in the vicinity of the corners ($h/256$). The price to pay for the integration is an increase of one order of magnitude of the number of integration points. If the target error level is near 10^{-3}, then coarser octree meshes can be selected ($h_g = h/64$ is sufficient here). Nonetheless, the same error level can be obtained if an anisotropic integration mesh is used: in this case, the number of integration points can be reduced by one order of magnitude. Similar conclusions can be drawn for larger target error levels.

In conclusion, we have demonstrated that the use on the anisotropic integration strategy enables to save a large number of integration cells if the interface contains both low and large curvature zones (which is the case for a large number of industrial structures). On the contrary, the benefits of the anisotropic strategy are smaller when constant curvature zones are considered (see Sections 2.4 and 3.1.1). Yet, in all cases the strategy is at least as efficient as octree integration. In addition, the method works "top to bottom" in contrast to the octree: it enables to capture small features that could be lost by the octree (below the resolution of the maximal depth).

3.2 2D Thin structures

Thanks to its features, the proposed method is well adapted if thin structures are of interest. As these slender geometries can be represented accurately and efficiently, we try to assess fully three-dimensional fictitious domain strategies for such structures. The

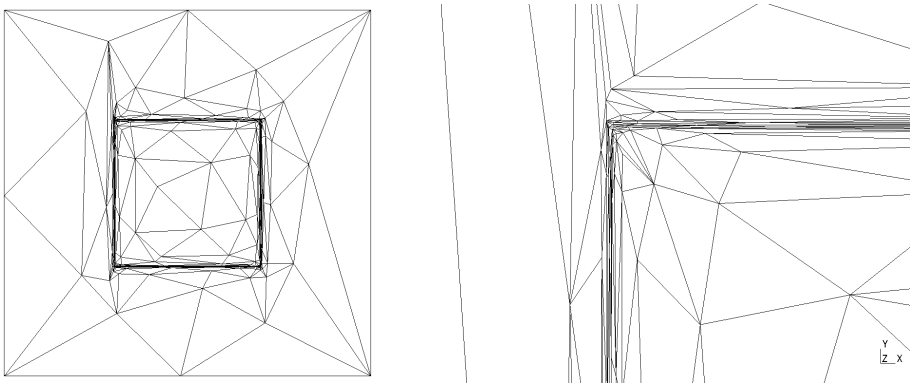

Figure 15: Kinked interface: anisotropic mesh (639 nodes, $\varepsilon = 10^{-4}$).

salient benefits are the ease of meshing, the possibility to handle true three-dimensional solutions with simple transition between thin and massive zones and general nonlinear models. As locking is the main difficulty for solid-shell methods, we focus on the robustness of the method with respect to locking by applying the method to classical test-cases from the literature.

3.2.1 Quarter circle beam

Consider a quarter circle beam as depicted in Figure 16(a). If the width of the beam is assumed to be small, then the problem can be solved in 2D (on the cross-section) with the plane stress assumption. Such geometry is prone to locking when discretized with classical solid finite elements. The beam is blocked at its bottom face and a unit vertical load is distributed on the left face. The radius of the beam is kept fixed whereas the thickness h is set to $R/10$, $R/100$ or $R/1000$, which correspond respectively to slenderness ratios of 10, 100 and 1000. Solving this problem with a Timoshenko beam model gives the following deflection:

$$u_y^{ref} = \frac{F\,R\,h^2}{\mu\,b} + \frac{3\,F\pi\,R^3}{E\,b}, \tag{3}$$

where μ is the shear modulus, E Young's modulus and b the width of the beam. The problem is solved by means of fictitious domain method with the anisotropic integration algorithm. The resulting integration meshes for the slenderness ratios given above are presented in Figure 17. All meshes were designed with a regularization parameter $\varepsilon = 10^{-6}$ and a target of 1100 nodes for the two smaller thickness ratios, and 1500 nodes for the thinnest geometry.

The approximation mesh is kept fixed with 16×16 hierarchical elements in the bounding box of the beam. The corresponding remaining cells are presented in Figure 18. A p convergence is conducted with p from 1 to 8, and the vertical displacement on the

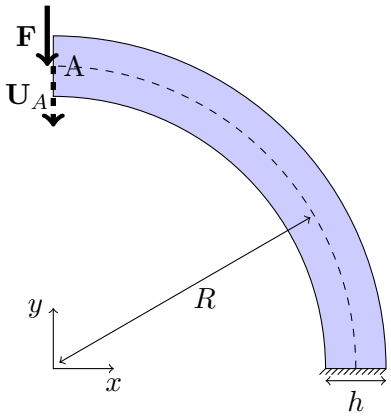

Figure 16: Quarter circle beam: problem description

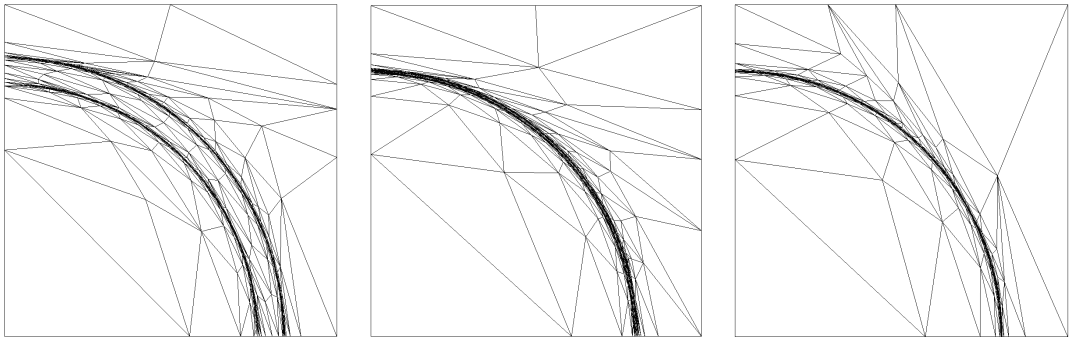

Figure 17: Geometrical meshes: from left to right 1087, 1099 and 1581 nodes.

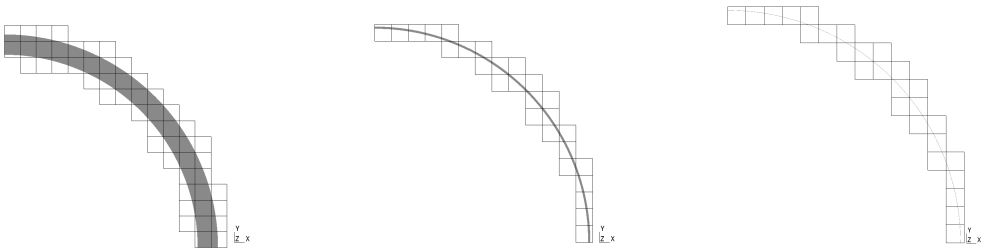

Figure 18: Elements containing matter for slenderness ratios of 10, 100 and 1000.

left edge of the beam is monitored. The corresponding results are compared to the reference solution in Figure 19. It can be seen that the convergence of the displacement towards the reference solution is very fast, and almost not influenced by the slenderness ratio. Note also that such a problem could be solved by means of conforming high-order elements [64] or isogeometric elements [54].

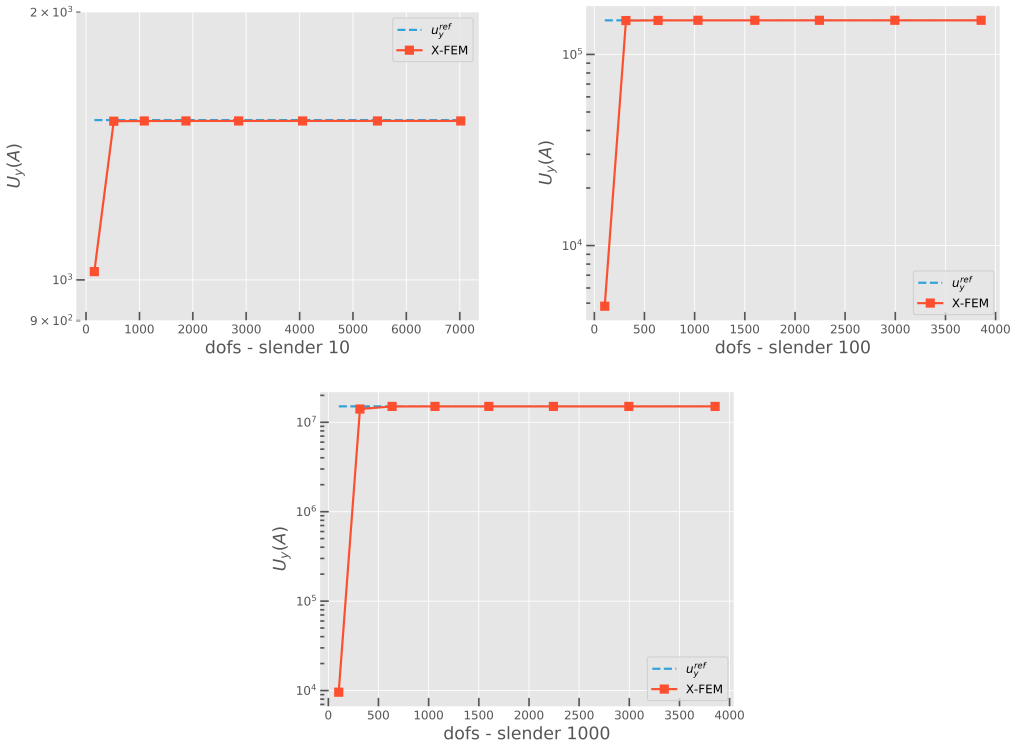

Figure 19: Convergence of the displacement for slenderness ratios of 10, 100 and 1000.

3.2.2 A discussion on conditioning

The influence on the condition number of the finite element operator is now discussed. Consider the problem of a clamped beam of width t depicted in Figure 20a. The beam is immersed in a mesh composed of 16×1 or 16×3 quadrangular elements, depending on its slenderness. A hierarchical Legendre approximation is defined on these elements, and the evolution of the condition number of the operator against the increase of the slenderness of the beam L/t is monitored during p-refinement ($p = 1 \cdots 6$). The condition number of the operator $\kappa(\mathbf{A}) = \lambda_{\max}/\lambda_{\min}$ is computed through the evaluation of the extreme eigenvalues of $\mathbf{A}$, $\lambda_{\max}$ and $\lambda_{\min}$. These eigenvalues are computed by means of an implicitly restarted Arnoldi iterations algorithm [65]. Note that a Shift and Invert algorithm is used to estimate efficiently $\lambda_{\min}$: Rather than finding this minimal

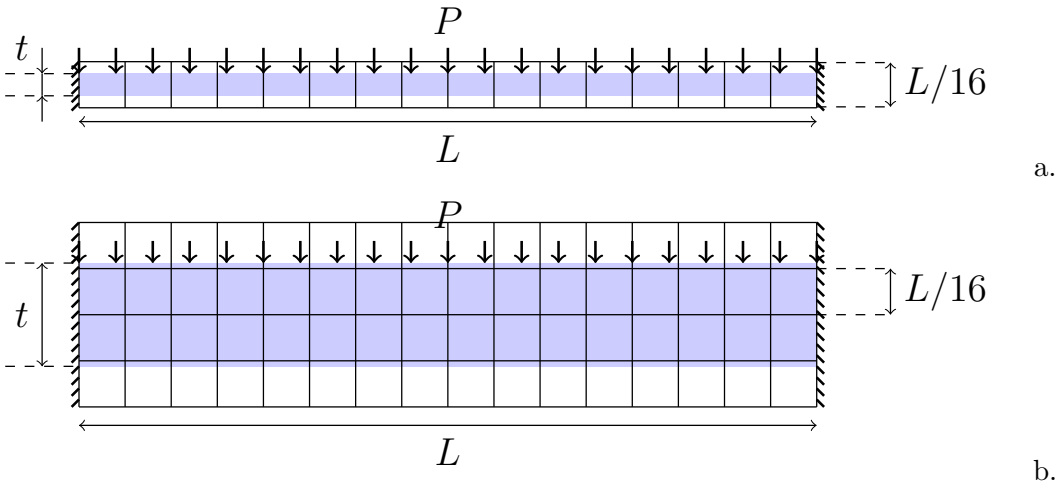

Figure 20: Problem for the conditioning study. High slenderness ratio (top) and low slenderness ratio (bottom).

eigenvalue, the following modified eigenvalue problem is considered: $(\mathbf{A} - \sigma\mathbf{I})^{-1}\mathbf{x} = \nu\mathbf{x}$, where σ is close to $\lambda_{\min}$, and $\nu = 1/(\lambda_{min} - \sigma)$. This strategy enhances the convergence of the algorithm to the desired portion of the spectrum.

The evolution of the condition number is depicted in Figure 21 (a). The impact of the slenderness ratio L/t is clearly seen, as although large slenderness can be considered (up to 1000), the condition number increases at a rate which is clearly linked to L/t. For slenderness ratios larger 200, round-off errors prevent to compute accurately $\lambda_{\min}$ when $p > 4$ (this is due to the inverse of $\mathbf{A}$ that appears in the Shift and Invert eigenvalue problem), so that the polynomial range for plotting is reduced. It has to be noted that $p = 4$ led to converged (in 2D) or almost converged results (in 3D) for all the numerical examples presented in this paper. It is also interesting to mention that slenderness is not the only cause of these conditioning issues: massive beams can also lead to very large condition number (see Figure 20b for the example of a beam with $L/t = 7.9$). This behaviour is discussed carefully in [66] where the authors have shown that the large condition number of Finite-Cell operators can be linked either to a large discrepancy in the volumic fraction of the approximation elements (see Figure 20b), or to the quasi-linear dependency of the polynomial basis (which tends to become the primary cause of conditioning issues for slender structures as in Figure 20a).

Preconditioning strategies, such as diagonal scaling can efficiently cure the first cause, but not the second one. De Prenter et al. proposed a Symmetric Incomplete Permuted Inverse Cholesky preconditioner (SIPIC) [66] that can efficiently precondition for both volumic fraction and quasi-linear dependency issues. Although this preconditioning strategy is not used in this next examples of the paper, we are currently investigating its use. An initial characterization of the performances of the preconditioner is presented in Figure 21 (b). It can be seen that SIPIC preconditioner successfully improves the

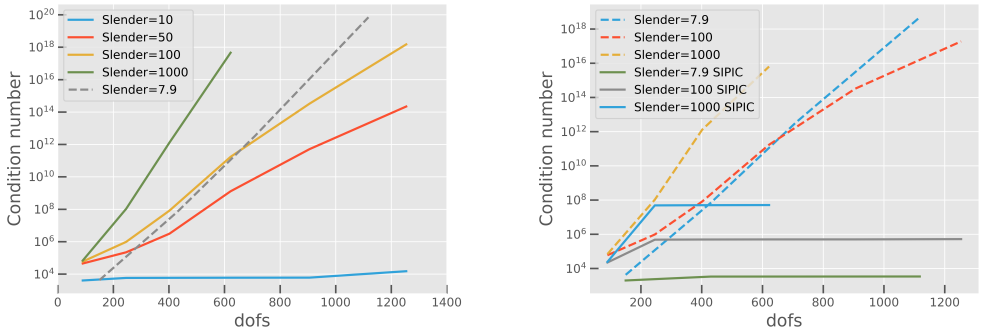

(a) (b)

Figure 21: Evolution of the condition number for p-refinement ($p = 1 \cdots 6$). (a) no preconditioning; (b) SIPIC preconditioner

condition number for our problem. The preconditioner is very efficient and leads to an almost constant condition number independently of the order of the approximation (for Legendre basis). The preconditioner is finally compared against classical preconditioners for two different slenderness ratios in Figure 22 (Jacobi and Incomplete Cholesky with preserved sparsity, see [66] for the setup of the preconditioners). It can be seen that SIPIC preconditioner is to be very robust, although is seems sometimes less efficient than the incomplete Cholesky preconditioner. Nevertheless, in every case the sparsity of the SIPIC preconditioner is far better than for the incomplete Cholesky preconditioner, see Figure 23.

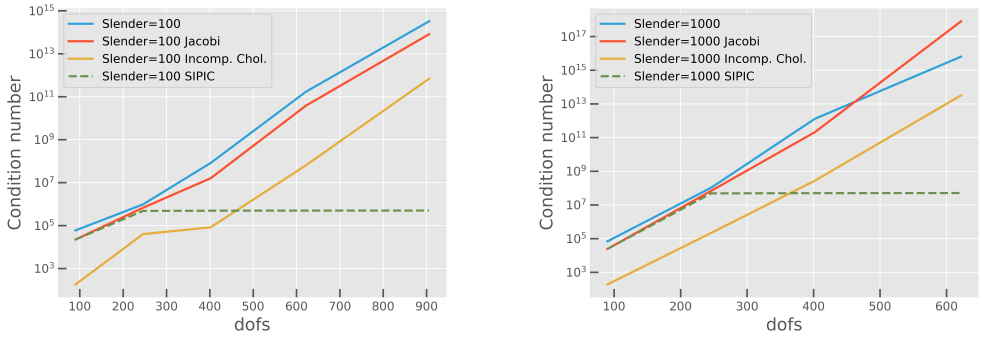

(a) (b)

Figure 22: Comparison of the performance of various preconditioning strategies during p-refinement ($p = 1 \cdots 6$). (a) Slenderness = 100; (b) Slenderness = 1000

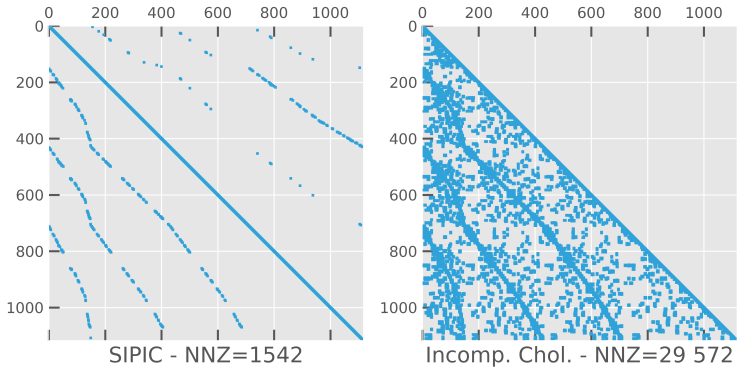

Figure 23: Comparison of the sparsity pattern of SIPIC and Incomplete Cholesky preconditioner (with preservation of the sparsity pattern) for a slenderness ratio of 7.9 $p = 4$.

3.3 3D thin structures

3.3.1 Scordelis-Lo roof

Consider the Scordelis-Lo roof [67] with dead load benchmark which is depicted in Figure 24. The geometrical and material properties are taken from [68]. This problem is a well known benchmark problem to assess the performances of shell and solid-shell elements. We want to treat this problem by means of the X-FEM, in order to study whether the anisotropic meshing algorithm is able to capture accurately the geometry of the roof and also its sensitivity to locking.

Due to symmetries, only one fourth of the roof is modelled, and the end diaphragm is considered as rigid. The regularization parameter of the anisotropic algorithm is set to 5.10^{-2} which is 40 times smaller than the thickness of the roof. The resulting mesh, which contains 18 150 nodes is depicted in Figure 25.

The computational mesh and the iso-zero of the level-set representing the geometry are shown in Figure 26: notice how coarse the mesh with respect to the geometry is.

A p convergence is conducted ($p = 1 \cdots 5$), and both strain energy and displacement at point A (see Figure 24) are monitored. Two computational meshes are considered: one with $2 \times 2 \times 2$ elements (as depicted in Figure 26(a)) and one with $8 \times 8 \times 8$ elements. The vertical displacement at point A is compared to the reference value 0.00885 [67], and the strain energy to the reference value given in [68]: $U_{ref} = 0.003933076912$. The corresponding displacement field is depicted in Figure 26(b) for various polynomial orders.

The evolution of the displacement at point A is presented in Figure 27 (a): Even the coarsest mesh converges to the reference solution for low polynomial orders (cubic) and with less than 2000 dofs. Concerning the convergence of the relative error in the energy norm (Figure 27 (b)), very low error levels can be attained with nearly exponential

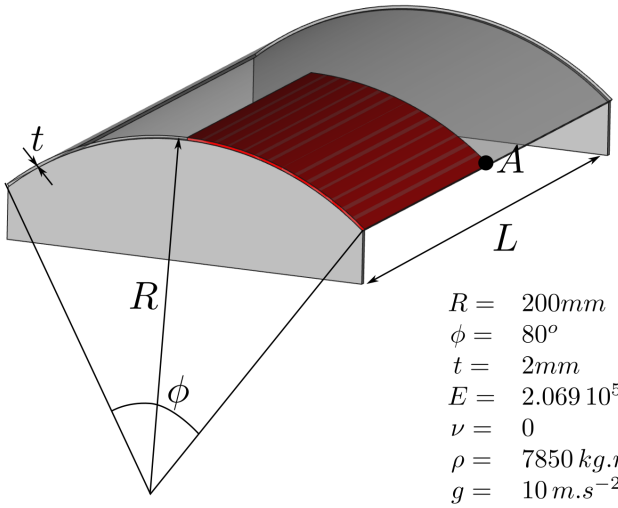

Figure 24: Scordelis-Lo roof with dead load benchmark problem

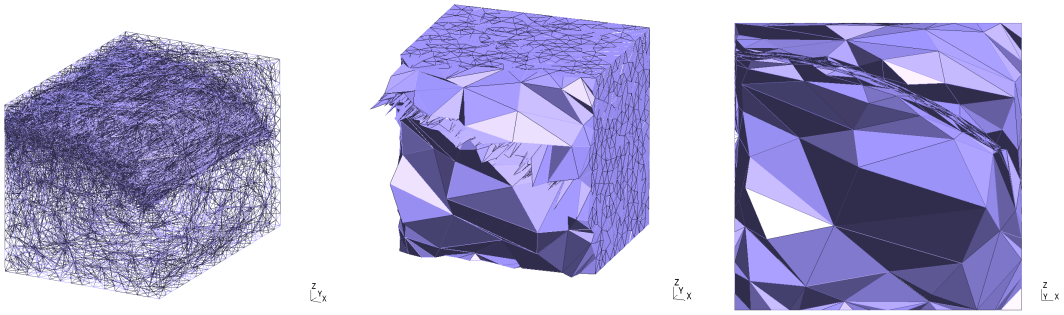

Figure 25: Anisotropic geometrical mesh.

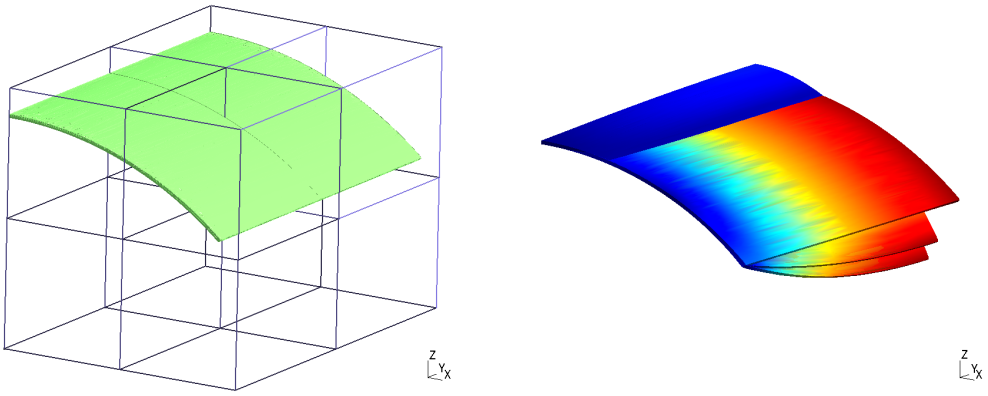

(a) (b)

Figure 26: Scordelis-Lo roof: (a) Computational mesh and geometry; (b) deformed configuration for $p = 1, 2$ and 3

convergence in the pre-asymptotic range.

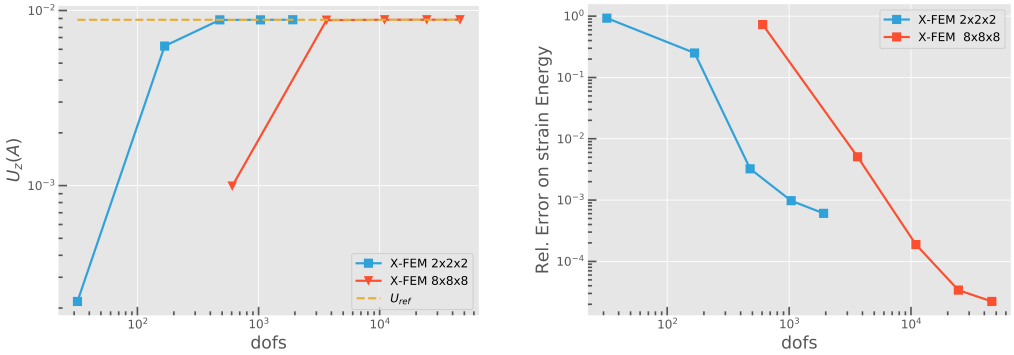

(a) (b)

Figure 27: Scordelis-Lo roof: (a) Convergence of $U_z(A)$; (b) Convergence of the strain energy.

3.3.2 Twisted beam

Consider the Twisted Beam problem proposed in [67], and illustrated in Figure 28. The beam is clamped on one end, and subjected to an out-of-plane loading on the opposite face (uniform tractions). This problem is known to be a severe test for assessing shell elements performance. Following [56], two beam thickness are considered $h = 0.32$ and $h = 0.0032$, for the so-called thick and thin cases respectively. Reference displacements

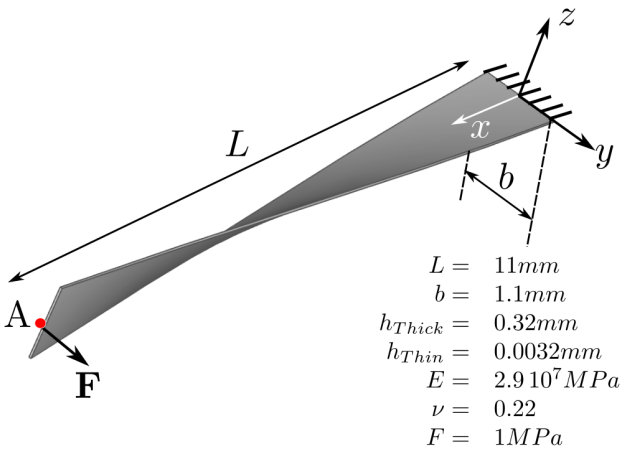

Figure 28: Twisted beam: geometry and boundary conditions.

at the center of the free end of the beam are given in [67]. The problem is solved on the very coarse meshes depicted in Figure 29 by increasing the polynomial order.

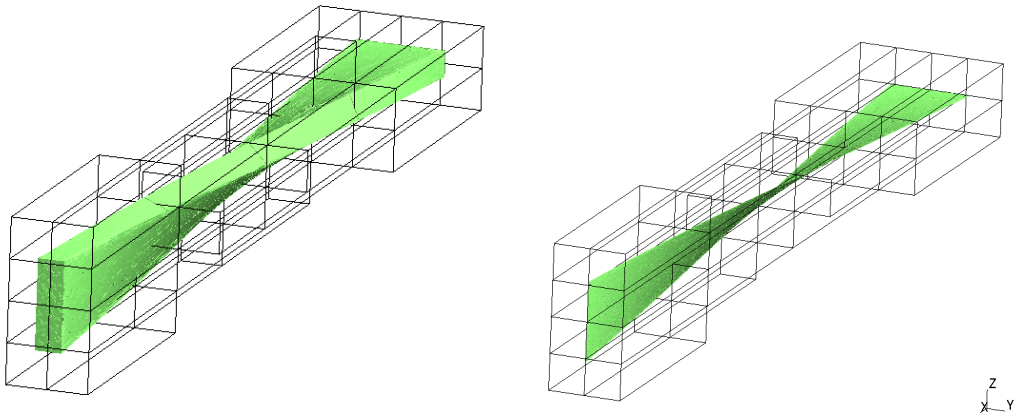

Figure 29: Twisted beam: Geometry and approximation meshes.

Anisotropic integration meshes (see figures 31 and 32) are obtained from very coarse meshes such the one presented in Figure 30, and by means of a regularization parameter of 10^{-3}.

Typical (non smoothed) von Mises stress fields are depicted in figures 33 and 34 for the thick and thin cases respectively.

The convergence of the displacement of center of the free end section is presented in Figure 35, and compared to the reference solution. For the thick case, a very fast

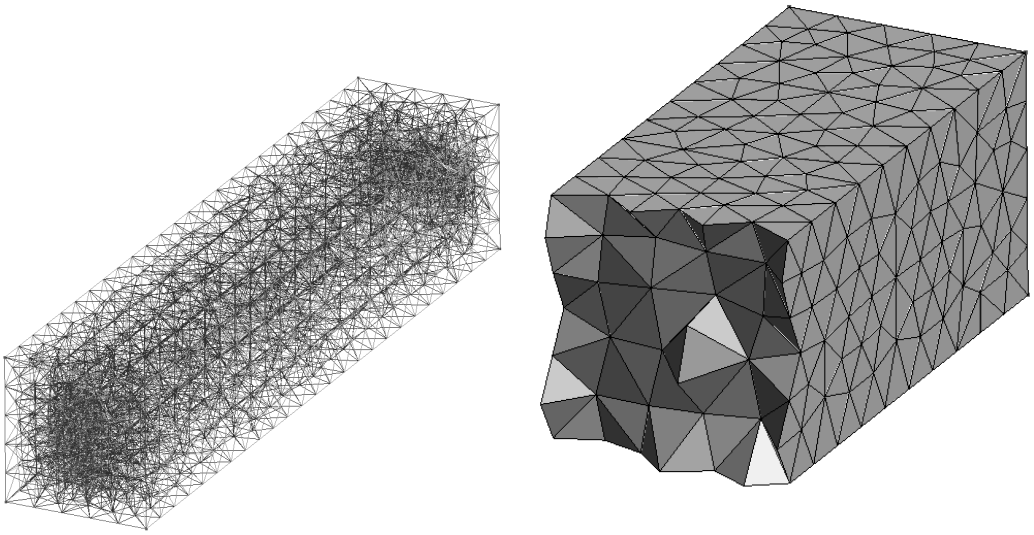

Figure 30: Twisted beam: Initial geometrical mesh before adaptation.

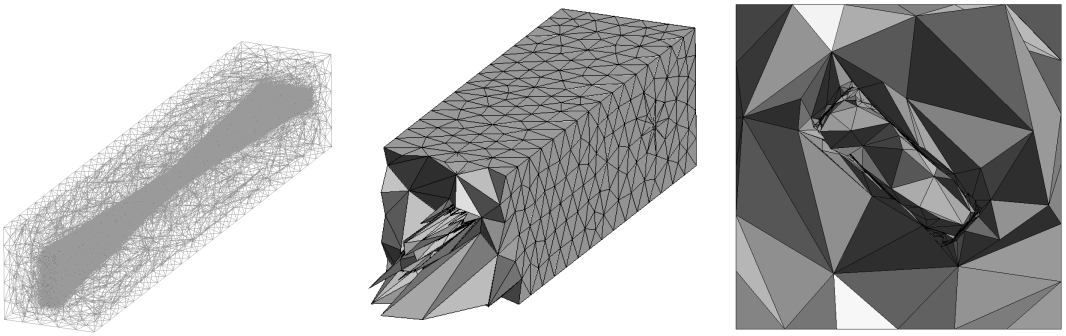

Figure 31: Twisted beam: anisotropic meshes for the thick beam ($\varepsilon = 10^{-3}$).

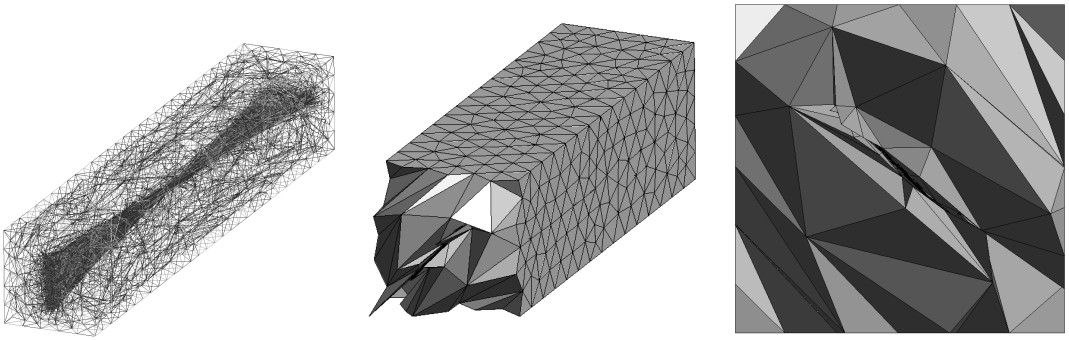

Figure 32: Twisted beam: anisotropic meshes for the thin beam ($\varepsilon = 10^{-3}$).

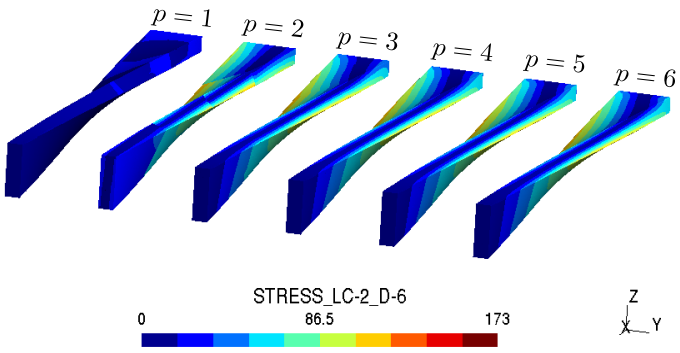

Figure 33: Twisted beam: von Mises stress field (left to right: increasing polynomial order)

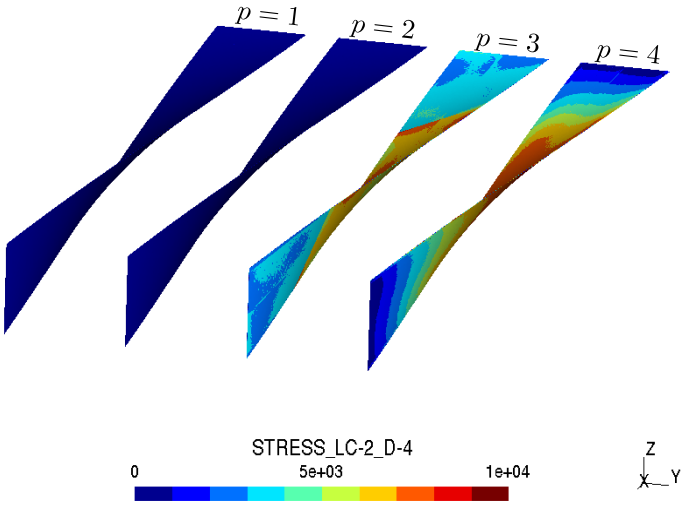

Figure 34: Twisted beam: von Mises stress field (left to right: increasing polynomial order)

convergence is observed (for $p \geq 3$), whereas the convergence is slower for the thin beam (for $p \geq 4$). Yet, convergence is still very fast. For the thin beam, the use of one unique element was also tested with a very good efficiency.

3.4 Three dimensional stiffened panel

As a more realistic example, consider the stiffened panel presented in Figure 36. The general dimensions of the panel are 600×1000mm, and its thickness is 2.944mm. The panel is blocked along its y and z outer boundaries, and subjected to a constant pressure P on its top face. The geometry is captured by means of an anisotropic mesh composed of 64000 nodes presented in Figure 37. The regularization parameter ε was set to 10^{-1}, and the bounding box of the mesh is $600 \times 600 \times 1000$mm.

Next, a p convergence is conducted, and both displacement and strain energy are compared to an overkill quadratic solid finite element computation involving 500 000 dofs.

The mechanical problem is solved on a regular grid composed of 16 elements along each side of the cube. The associated computational mesh is represented in Figure 38. Displacement and stress fields are compared for both computations (with $p = 4$ approximation) in Figure 39, and it can be seen that they both agree very well although the fictitious domain calculation only involves 21 000 dofs.

The corresponding convergences are depicted in Figure 40. It can be seen than both displacement and energy converge to the reference solution with no meshing burden. However, Figure 40 (b) also highlights a slower convergence rate than in the previous examples. This could be related to the geometrical accuracy that may deviate the results from the reference solution or to conditioning issues that may hinder the accuracy.

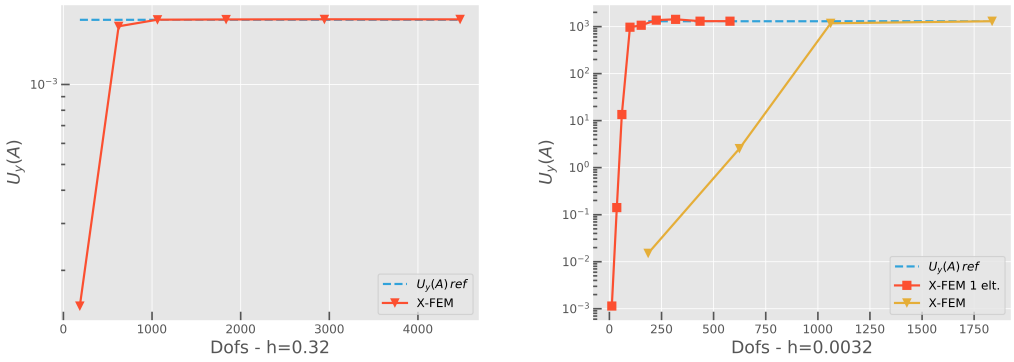

Figure 35: Twisted beam: Convergence of the displacement field at the center of the end section. (a) Thick beam; (b) Thin beam.

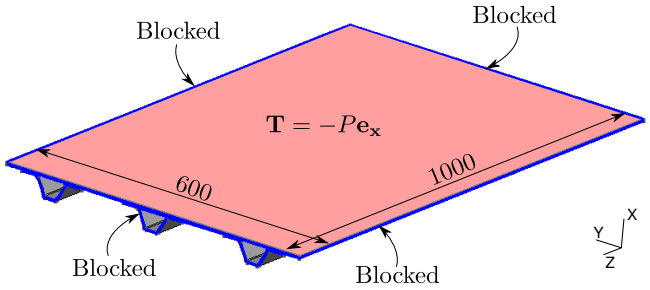

Figure 36: Stiffened panel: dimensions and boundary conditions (in blue: fixed boundary; in red: uniform pressure).

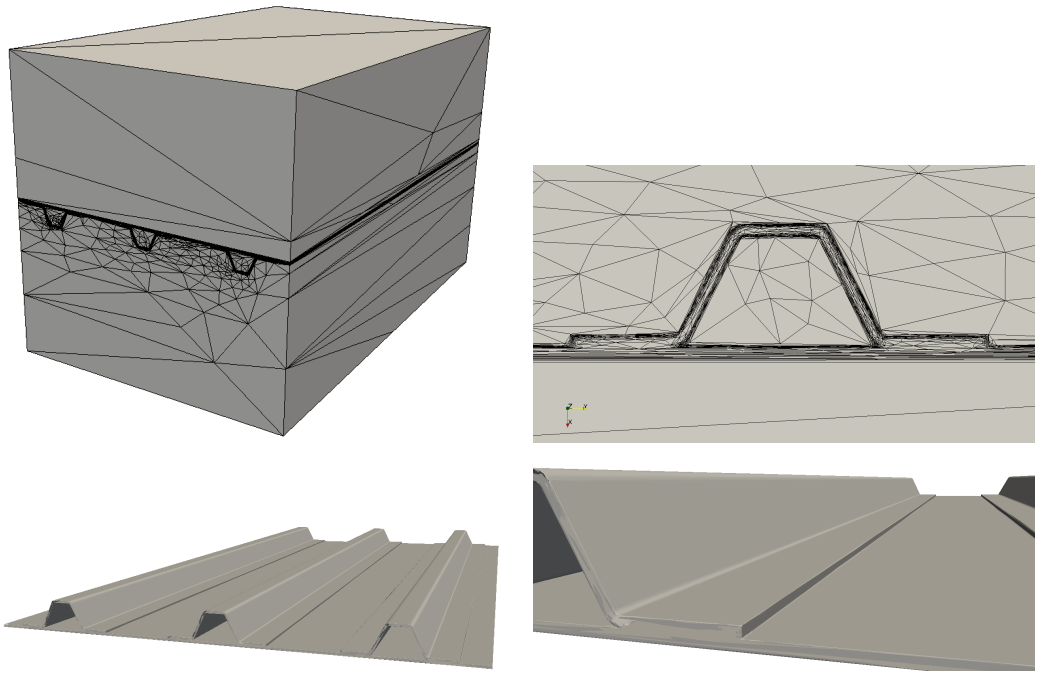

Figure 37: Stiffened panel: geometrical mesh (64000 nodes) and corresponding level-set iso zero.

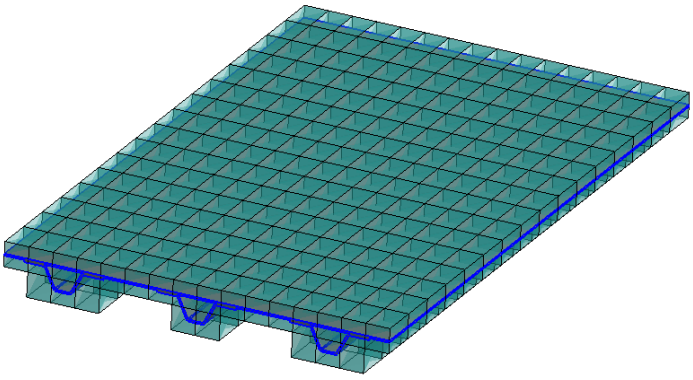

Figure 38: Stiffened panel: computational mesh.

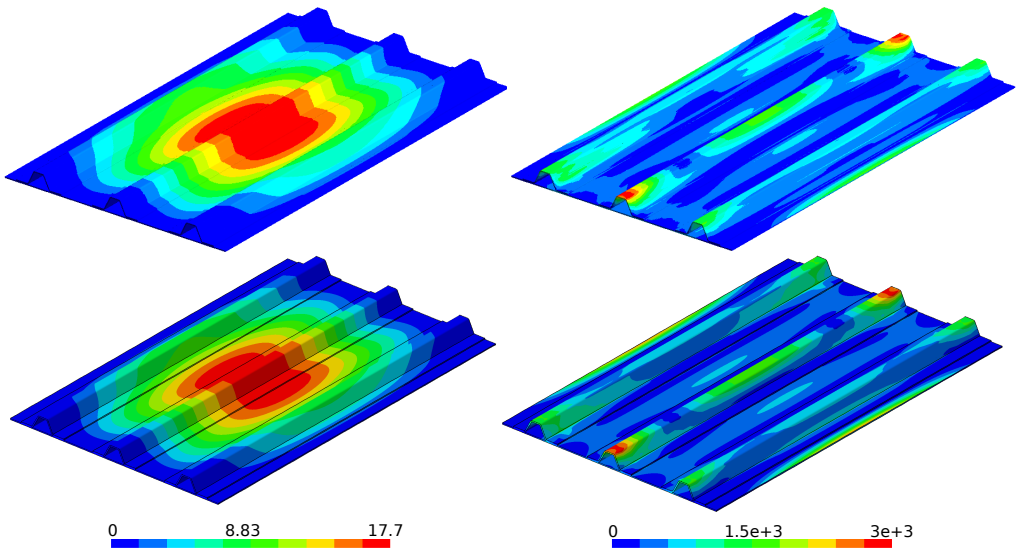

Figure 39: Stiffened panel: comparison between the $p = 4$ computation (top) and the reference solution (bottom). Left: displacement, right: von Mises norm of the stress field. Note that the discrepancy between these two solutions is magnified here as the stress field is assumed to be linear on each element in the fictitious domains case (it is cubic in reality).

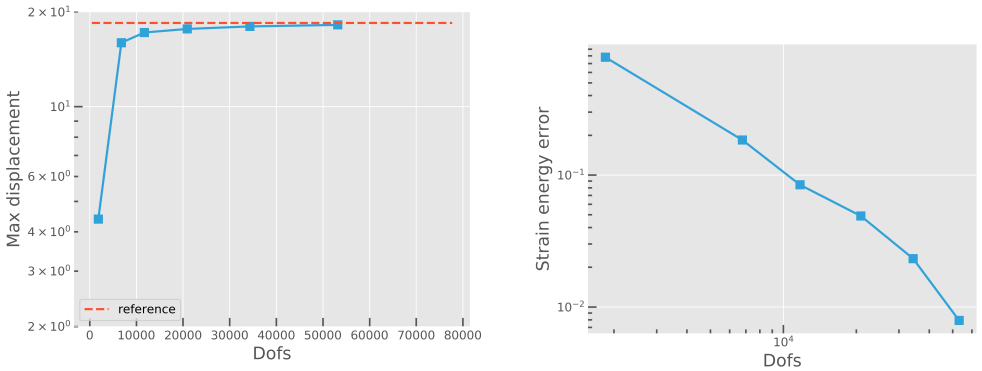

(a) (b)

Figure 40: Stiffened panel: (a) Evolution of the maximal displacement on the structure; (b) Approximation mesh; (c) Convergence of the strain energy error.

3.4.1 Ribbed Corner

The aim of this last example is to highlight the performance of the method for geometries involving both massive and thin areas. A ribbed corner, as depicted in Figure 41 (a) is considered. This part is made of a linear elastic material with a 200 000 MPa Young's modulus and a 0.3 Poisson's ratio. The bottom face of the part is fixed, and surface tractions are applied on its extreme $\vec{x}$ face. The approximation and adapted geometrical

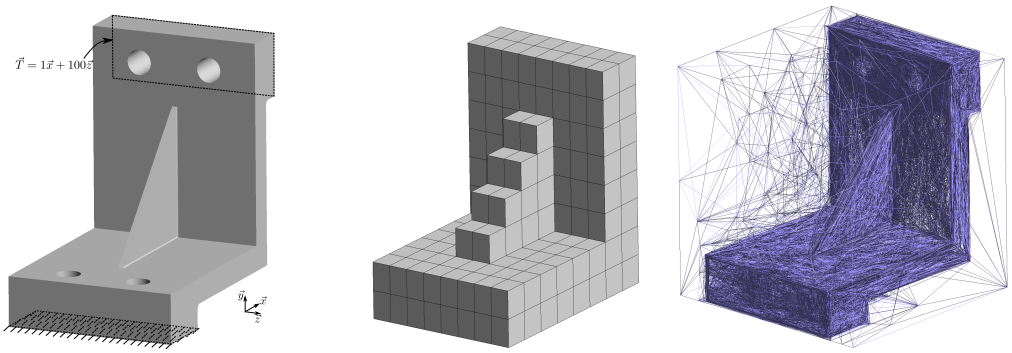

(a) (b) (c)

Figure 41: Ribbed corner: (a) Geometry and boundary conditions; (b) Adapted geometrical mesh (390 473 nodes)

meshes are shown in Figures 41 (b) and (c) respectively. The evolution of displacement and stresses during the elevation of the polynomial order are presented in Figure 42. It can be seen that the proposed approach is able to treat seamlessly both thin and thick areas of the part. The evolution of the strain energy during p refinement is presented in Figure 43. Comparison is made with a linear conforming finite element approximation with increasing number of elements, and an overkill conforming finite element solution (1 765 101 dofs) which serves as reference. It can be seen that two orders of magnitudes can be saved for a given accuracy, with respect to the direct finite element calculations. Note here that the combination of the proposed method with octree refinement near re-entrant corners would certainly improve the convergence.

4 Conclusion

An efficient integration method has been proposed in the context of fictitious domain methods. It relies on an edge-based error estimator and an associated metric field that drives an anisotropic mesh adaptation procedure. In 2D, it has been shown that for a given accuracy, this approach could lead to one order of magnitude less integration points compared to classical sub-grid based integration strategies. This occurs especially when the interfaces exhibit both low and large curvatures, which is common for industrial structures. For more homogeneous curvatures, the approach was demonstrated to

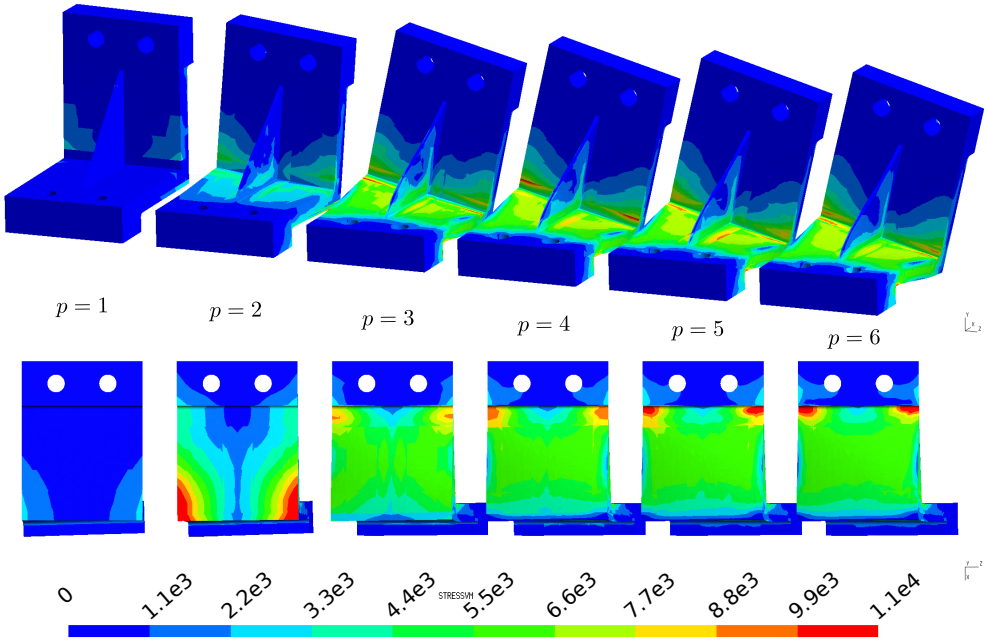

Figure 42: Ribbed corner: Evolution of the mechanical fields during p convergence. From left to right: $p = 1$,2, 3, 4, 5 and 6.)

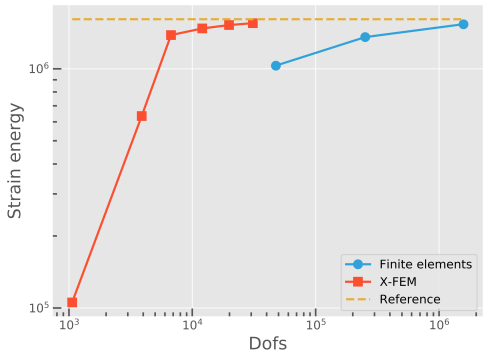

Figure 43: Ribbed corner: Evolution of the strain energy during p refinement, and comparison with conforming F.E. computations.)

be as least as accurate as subgrid-based integration schemes. Finally, it is important to note that this approach is top to bottom, which make it possible to discover very small features that could not be represented by the subgrid scheme if it falls below its spatial minimal resolution. It has been shown that thanks to this flexible tool, high-order fictitious domain methods could be used as solid-shell methods, handling naturally thin, solid regions and their connection. Numerical examples have demonstrated that locking-free and computationally efficient solutions could be obtained for classical benchmarks. Still, additional work should be conducted to further improve the approach: mesh refinement strategies at the approximation level should be considered in order to capture local stress concentrations, while improving the conditioning of the operators is of primary importance if iterative solvers are used. The strategy proposed here extends naturally with tree-based approximation grids to handle the first issue, whereas preliminary results indicate that the preconditioner proposed in [66] seems to be a promising approach.

Acknowledgements:
The support of the ERC Grant XLS N ° 291102 is gratefully acknowledged.
The authors would like to thank F. de Prenter for letting an implementation of the SIPIC preconditioner available.

References

[1] D. Schillinger, L. Dedè, M. a. Scott, J. a. Evans, M. J. Borden, E. Rank, and T. J. R. Hughes. An isogeometric design-through-analysis methodology based on adaptive hierarchical refinement of NURBS, immersed boundary methods, and T-spline CAD surfaces. *Computer Methods in Applied Mechanics and Engineering*, 249-252:116–150, 2012.

[2] J. Cottrell, T. J. R. Hughes, and Y. Bazilevs. *Isogeometric Analysis*. 2009.

[3] H.-J. Kim, Y.-D. Seo, and S.-K. Youn. Isogeometric analysis for trimmed CAD surfaces. *Computer Methods in Applied Mechanics and Engineering*, 198(37-40):2982–2995, aug 2009.

[4] E. Rank, M. Ruess, S. Kollmannsberger, D. Schillinger, and A. Düster. Geometric modeling, isogeometric analysis and the finite cell method. *Computer Methods in Applied Mechanics and Engineering*, 249-252:104–115, dec 2012.

[5] G. Beer, B. Marussig, and J. Zechner. A simple approach to the numerical simulation with trimmed CAD surfaces. *Computer Methods in Applied Mechanics and Engineering*, 285:776–790, 2015.

[6] M. Ruess, D. Schillinger, A. I. Özcan, and E. Rank. Weak coupling for isogeometric analysis of non-matching and trimmed multi-patch geometries. *Computer Methods in Applied Mechanics and Engineering*, 269:46–71, feb 2014.

[7] S. Kollmannsberger, A. I. Özcan, J. Baiges, M. Ruess, E. Rank, and A. Reali. Parameter-free, weak imposition of Dirichlet boundary conditions and coupling of trimmed and non-conforming patches. *International Journal for Numerical Methods in Engineering*, 101(9):670–699, dec 2014.

[8] A. P. Nagy and D. J. Benson. On the numerical integration of trimmed isogeometric elements. *Computer Methods in Applied Mechanics and Engineering*, 284:165–185, 2015.

[9] V. K. Saulèv. On the solution of some boundary value problems on high performance computers by fictitious domain method. *Siberian Math. J.*, 4:912–925, 1963.

[10] T. Belytschko, C. Parimi, N. Moës, N. Sukumar, and S. Usui. Structured extended finite element methods for solids defined by implicit surfaces. *International Journal for Numerical Methods in Engineering*, 56(4):609–635, jan 2003.

[11] G. Legrain, P. Cartraud, I. Perreard, and N. Moës. An X-FEM and level set computational approach for image-based modelling: Application to homogenization. *International Journal for Numerical Methods in Engineering*, 86(7):915–934, 2010.

[12] W. Lian, G. Legrain, and P. Cartraud. Image-based computational homogenization and localization: comparison between X-FEM/levelset and voxel-based approaches. *Computational Mechanics*, 51(3):279–293, may 2013.

[13] G. Legrain and N. Moës. Treatment of nearly-singular problems with the X-FEM. *Advanced Modeling and Simulation in Engineering Sciences*, 1(1):13, dec 2014.

[14] G. Legrain, N. Chevaugeon, and K. Dréau. High order X-FEM and levelsets for complex microstructures: Uncoupling geometry and approximation. *Computer Methods in Applied Mechanics and Engineering*, 241-244:172–189, oct 2012.

[15] G. Legrain, C. Geuzaine, J.-F. Remacle, N. Moës, P. Cresta, and J. Gaudin. Numerical simulation of CAD thin structures using the eXtended Finite Element Method and Level Sets. *Finite Elements in Analysis and Design*, 77:40–58, 2013.

[16] E. Nadal, J. J. Ródenas, J. Albelda, M. Tur, J. E. Tarancón, and F. J. Fuenmayor. Efficient Finite Element Methodology Based on Cartesian Grids: Application to Structural Shape Optimization. *Abstract and Applied Analysis*, 2013:1–19, 2013.

[17] A. Düster, J. Parivizian, Z. Yang, and E. Rank. The finite cell method for three-dimensional problems of solid mechanics. *Computer Methods in Applied Mechanics and Engineering*, 197(45-48):3768–3782, aug 2008.

[18] E. Rank, S. Kollmannsberger, C. Sorger, and A. Düster. Shell Finite Cell Method: A high order fictitious domain approach for thin-walled structures. *Computer Methods in Applied Mechanics and Engineering*, 200(45-46):3200–3209, oct 2011.

[19] J. Parvizian, A. Düster, and E. Rank. Finite cell method - h and p extension for embedded domain problems in solid mechanics. *Computational Mechanics*, 41(1):121–133, 2007.

[20] A. Düster, H.-G. Sehlhorst, and E. Rank. Numerical homogenization of heterogeneous and cellular materials utilizing the finite cell method. *Computational Mechanics*, 50(4):413–431, jan 2012.

[21] D. Schillinger, M. Ruess, N. Zander, Y. Bazilevs, A. Düster, and E. Rank. Small and large deformation analysis with the p- and B-spline versions of the Finite Cell Method. *Computational Mechanics*, 50(4):445–478, feb 2012.

[22] D. Schillinger and E. Rank. An unfitted hp-adaptive finite element method based on hierarchical B-splines for interface problems of complex geometry. *Computer Methods in Applied Mechanics and Engineering*, 200(47-48):3358–3380, 2011.

[23] K. Dréau, N. Chevaugeon, and N. Moës. Studied X-FEM enrichment to handle material interfaces with higher order finite element. *Computer Methods in Applied Mechanics and Engineering*, 199(29-32):1922–1936, jun 2010.

[24] Z. Yang, M. Ruess, S. Kollmannsberger, and E. Rank. An efficient integration technique for the voxel-based finite cell method. *International Journal for Numerical Methods in Engineering*, (June):457–471, 2012.

[25] S. E. Mousavi and N. Sukumar. Numerical integration of polynomials and discontinuous functions on irregular convex polygons and polyhedrons. *Computational Mechanics*, 47(5):535–554, dec 2010.

[26] Y. Sudhakar and W. A. Wall. Quadrature schemes for arbitrary convex/concave volumes and integration of weak form in enriched partition of unity methods. *Computer Methods in Applied Mechanics and Engineering*, 258:39–54, may 2013.

[27] B. Müller, F. Kummer, and M. Oberlack. Highly accurate surface and volume integration on implicit domains by means of moment-fitting. *International Journal for Numerical Methods in Engineering*, 96(8):512–528, nov 2013.

[28] M. Joulaian, S. Hubrich, and A. Düster. Numerical integration of discontinuities on arbitrary domains based on moment fitting. *Computational Mechanics*, 4(C), mar 2016.

[29] J. N. Lyness and D. Jespersen. Moderate Degree Symmetric Quadrature Rules for the Triangle. *IMA Journal of Applied Mathematics*, 15(1):19–32, 1975.

[30] J. N. Lyness and G. Monegato. Quadrature Rules for Regions Having Regular Hexagonal Symmetry. *SIAM Journal on Numerical Analysis*, 14(2):283–295, apr 1977.

[31] D. A. Dunavant. High degree efficient symmetrical Gaussian quadrature rules for the triangle. *International Journal for Numerical Methods in Engineering*, 21(6):1129–1148, jun 1985.

[32] T. Strouboulis and K. Copps. The Generalized Finite Element Method: An Example of its Implementation and Illustration of its Performance. *International Journal for Numerical Methods in Engineering*, 47(8):1401–1417, 2000.

[33] G. Legrain. A NURBS enhanced extended finite element approach for unfitted CAD analysis. *Computational Mechanics*, 52(4):913–929, apr 2013.

[34] O. Marco, R. Sevilla, Y. J. Zhang, J. J. Ródenas, and M. Tur. Exact 3D boundary representation in finite element analysis based on Cartesian grids independent of the geometry. *International Journal for Numerical Methods in Engineering*, 103(6):445–468, aug 2015.

[35] L. Kudela, N. Zander, T. Bog, S. Kollmannsberger, and E. Rank. Efficient and accurate numerical quadrature for immersed boundary methods. *Advanced Modeling and Simulation in Engineering Sciences*, 2(1):10, 2015.

[36] L. Kudela, N. Zander, S. Kollmannsberger, E. Rank, L. Kudela, N. Zander, S. Kollmannsberger, and E. Rank. Smart octrees: accurately integrating discontinuous functions in 3D. *Computer Methods in Applied Mechanics and Engineering*, To appear, 2016.

[37] T.-P. Fries and S. Omerović. Higher-order accurate integration of implicit geometries. *International Journal for Numerical Methods in Engineering*, 106(5):323–371, may 2016.

[38] P. J. Frey and P. L. George. *Mesh Generation: Application to Finite Elements*. Hermes Science Publishing Ltd;, 2000.

[39] W. Huang, L. Kamenski, and X. Li. Anisotropic Mesh Adaptation for Variational Problems Using Error Estimation Based on Hierarchical Bases. (Xianping Li).

[40] M. D. Piggott, P. E. Farrell, C. R. Wilson, G. J. Gorman, and C. C. Pain. Anisotropic mesh adaptivity for multi-scale ocean modelling. *Philosophical transactions. Series A, Mathematical, physical, and engineering sciences*, 367(1907):4591–4611, 2009.

[41] M. Picasso. Numerical study of the effectivity index for an anisotropic error indicator based on Zienkiewicz-Zhu error estimator. *Communications in Numerical Methods in Engineering*, 19(1):13–23, 2003.

[42] C. Bui, C. Dapogny, and P. Frey. An accurate anisotropic adaptation method for solving the level set advection equation. *International Journal for Numerical Methods in Fluids*, 70(7):899–922, 2012.

[43] Y. Bourgault and M. Picasso. Anisotropic error estimates and space adaptivity for a semidiscrete finite element approximation of the transient transport equation. *SIAM Journal on Scientific Computing*, 35(2):A1192–A1211, 2013.

[44] P. E. Farrell, S. Micheletti, and S. Perotto. An anisotropic Zienkiewicz-Zhu-type error estimator for 3D applications. *International Journal for Numerical Methods in Engineering*, 85(6):671–692, feb 2011.

[45] V. Ducrot and P. Frey. Anisotropic Level Set Adaptation for Accurate Interface Capturing. In *Proceedings of the 17th International Meshing Roundtable*, pages 159–176. Springer Berlin Heidelberg, Berlin, Heidelberg, 2008.

[46] R. Abgrall, H. Beaugendre, and C. Dobrzynski. An immersed boundary method using unstructured anisotropic mesh adaptation combined with level-sets and penalization techniques. *Journal of Computational Physics*, 257(PA):83–101, 2014.

[47] D.-L. Quan, T. Toulorge, E. Marchandise, J.-F. Remacle, and G. Bricteux. Anisotropic mesh adaptation with optimal convergence for finite elements using embedded geometries. *Computer Methods in Applied Mechanics and Engineering*, 268:65–81, jan 2014.

[48] T. Coupez. Metric construction by length distribution tensor and edge based error for anisotropic adaptive meshing. *Journal of Computational Physics*, 230(7):2391–2405, 2011.

[49] T. Coupez, L. Silva, and E. Hachem. Implicit Boundary and Adaptive Anisotropic Meshing. In *New Challenges in Grid Generation and Adaptivity for Scientific Computing*, pages 1–18. 2015.

[50] F. Abed-Meraim and A. Combescure. SHB8PS—a new adaptative, assumed-strain continuum mechanics shell element for impact analysis. *Computers & Structures*, 80(9-10):791–803, apr 2002.

[51] R. J. Alves de Sousa, R. P. Cardoso, R. A. Fontes Valente, J.-W. Yoon, J. J. Grácio, and R. M. Natal Jorge. A new one-point quadrature enhanced assumed strain (EAS) solid-shell element with multiple integration points along thickness: Part I-geometrically linear applications. *International Journal for Numerical Methods in Engineering*, 62(7):952–977, feb 2005.

[52] S. Reese. A large deformation solid-shell concept based on reduced integration with hourglass stabilization. *International Journal for Numerical Methods in Engineering*, 69(8):1671–1716, feb 2007.

[53] B. Bassa, F. Sabourin, and M. Brunet. A new nine-node solid-shell finite element using complete 3D constitutive laws. *International Journal for Numerical Methods in Engineering*, 92(7):589–636, nov 2012.

[54] R. Bouclier, T. Elguedj, and A. Combescure. On the development of NURBS-based isogeometric solid shell elements: 2D problems and preliminary extension to 3D. *Computational Mechanics*, 52:1085–1112, 2013.

[55] R. Bouclier, T. Elguedj, and A. Combescure. Efficient isogeometric NURBS-based solid-shell elements: Mixed formulation and Bbar-method. *Computer Methods in Applied Mechanics and Engineering*, 267:86–110, dec 2013.

[56] R. Bouclier, T. Elguedj, and A. Combescure. An isogeometric locking-free NURBS-based solid-shell element for geometrically nonlinear analysis. *International Journal for Numerical Methods in Engineering*, pages n/a–n/a, dec 2014.

[57] A. Düster, D. Scholz, and E. Rank. pq-Adaptive solid finite elements for three-dimensional plates and shells. *Computer Methods in Applied Mechanics and Engineering*, 197(1-4):243–254, dec 2007.

[58] P. J. Frey and F. Alauzet. Anisotropic mesh adaptation for CFD computations. *Computer Methods in Applied Mechanics and Engineering*, 194(48-49):5068–5082, 2005.

[59] S. G. Advani and C. L. Tucker III. The use of tensors to describe and predict fiber orientation in short fiber composites. *Journal of Rheology (1978-present)*, 31(8):751–784, 1987.

[60] A. Claisse, V. Ducrot, and P. J. Frey. Levelsets and anisotropic mesh adaptation. *Discrete and Continuous Dynamical Systems*, 23(1-2):165–183, 2009.

[61] T. Coupez and E. Hachem. Solution of high-Reynolds incompressible flow with stabilized finite element and adaptive anisotropic meshing. *Computer Methods in Applied Mechanics and Engineering*, 267:65–85, 2013.

[62] A. Abedian, J. Parvizian, A. Düster, H. Khademyzadeh, and E. Rank. Performance of Different Integration Schemes in Facing Discontinuities in the Finite Cell Method. *International Journal of Computational Methods*, 10(03):1350002, 2013.

[63] N. Sukumar, D. L. Chopp, N. Moës, and T. Belytschko. Modeling holes and inclusions by level sets in the extended finite-element method. *Computer Methods in Applied Mechanics and Engineering*, 190(46-47):6183–6200, 2001.

[64] A. Düster, H. Bröker, and E. Rank. The p-version of the finite element method for three-dimensional curved thin walled structures. *International Journal for Numerical Methods in Engineering*, 52(7):673–703, nov 2001.

[65] W. Arnoldi. The principle of minimized iterations in the solution of the matrix eigenvalue problem. *Quarterly of Applied Mathematics*, 9:17–29, 1951.

[66] F. de Prenter, C. V. Verhoosel, G. J. van Zwieten, and E. H. van Brummelen. Condition number analysis and preconditioning of the finite cell method. *Comput. Methods Appl. Mech. Engrg.*, (April), 2016.

[67] R. Macneal and R. Harder. A proposed standard set of problems to test finite element accuracy. *Finite elements in Analysis and Design*, 1:3–20, 1985.

[68] E. Rank, A. Düster, V. Nübel, K. Preusch, and O. Bruhns. High order finite elements for shells. *Computer Methods in Applied Mechanics and Engineering*, 194(21-24):2494–2512, jun 2005.